ADVANCED FUNCTIONAL MATERIALS
www.afm-journal.de

Spatially Immobilized PtPdFeCoNi as an Excellent Bifunctional Oxygen Electrocatalyst for Zinc–Air Battery

Mingkuan Xie, Yu Lu, Xin Xiao, Duojie Wu, Bing Shao, Hao Nian, Chunsheng Wu, Wenjuan Wang, Jun Gu, Songbai Han, Meng Gu, and Qiang Xu**

Developing efficient oxygen electrocatalysts with low cost, high catalytic activity, and robust stability remains a formidable challenge for rechargeable zinc–air batteries (ZABs). Herein, highly dispersed ultrasmall PtPdFeCoNi high-entropy alloy nanoparticles with a size of ≈ 2 nm and randomly distributed multimetallic single atoms spatially immobilized on the 3D hierarchically ordered porous nitrogen-doped carbon skeleton (denoted as PtPdFeCoNi/HOPNC) are successfully synthesized via ultra-rapid Joule heating process. The spatial immobilization on 3D HOPNC skeleton is the key to the high dispersion of multi-active sites of oxygen electrocatalysts, and the formed hierarchical pore structure is conducive to the successful construction of the rapid mass transfer channel. As a result, the as-prepared PtPdFeCoNi/HOPNC exhibits a positive half-wave potential of 0.866 V versus RHE for oxygen reduction reaction (ORR), a low overpotential of 310 mV at 10 mA cm^{-2} for oxygen evolution reaction (OER), and low Tafel slopes for both ORR and OER. Furthermore, ZAB using PtPdFeCoNi/HOPNC as bifunctional oxygen catalysts exhibits excellent rate performances and superior cycling stability, surpassing that of a commercial Pt/C-RuO_2 mixture. The spatial immobilization strategy of HOPNC provides a new idea for the design and synthesis of efficient catalysts for various applications.

1. Introduction

Advanced energy storage/conversion technologies are highly demanded for zero carbon emission and high energy conversion efficiency.[1] Rechargeable zinc–air batteries (ZABs) are regarded as one of the most promising electrochemical energy storage and conversion devices due to their low cost, high safety, environmental friendliness, and comparable theoretical energy density (1086 Wh kg^{-1}).[2] However, rechargeable ZABs still suffer from severe charge–discharge polarization and short cycle life owing to the sluggish oxygen reduction reaction (ORR) and oxygen evolution reaction (OER) kinetics and the poor stability of the air cathode.[3] To date, commercial noble metal-based materials (e.g., Pt, Pd, RuO_2, and IrO_2) are regarded as the benchmark electrocatalysts for either ORR or OER.[4] However, the high cost, limited mono-functionality, and poor stability obviously limit their large-scale applications in ZABs. Therefore, efficient bifunctional oxygen eletrocatalysts with low noble metal content, low cost, high catalytic activity, and robust stability are urgently required.

Electrocatalysts with dense active sites and open skeleton structures are of great importance. Recently, high-entropy alloys (HEAs) have sparked extensive attention due to their entropic effect, cocktail effect, lattice distortion, and sluggish diffusion effect, which enable them with superior catalytic activity and stability to traditional single metals or common alloys.[5] However, the sizes of most reported HEA nanoparticles (NPs) are larger than 10 nm, because high temperatures are usually required during the synthetic process, which inevitably accelerates the

M. Xie, Y. Lu, X. Xiao, B. Shao, H. Nian, C. Wu, W. Wang, Q. Xu
Shenzhen Key Laboratory of Micro/Nano-Porous Functional Materials (SKLPM)
Department of Chemistry
Department of Materials Science and Engineering
SUSTech-Kyoto University Advanced Energy Materials Joint Innovation Laboratory (SKAEM-JIL)
and Key University Laboratory of Highly Efficient Utilization of Solar Energy and Sustainable Development of Guangdong
Southern University of Science and Technology
Shenzhen 518055, P. R. China
E-mail: xiaox3@sustech.edu.cn; xuq@sustech.edu.cn, xu.qiang@icems.kyoto-u.ac.jp

The ORCID identification number(s) for the author(s) of this article can be found under https://doi.org/10.1002/adfm.202414537

D. Wu, M. Gu
Department of Materials Science and Engineering
Southern University of Science and Technology
Shenzhen 518055, P. R. China

J. Gu
Department of Chemistry
Southern University of Science and Technology
Shenzhen 518055, P. R. China

S. Han
Academy for Advanced Interdisciplinary Studies
Southern University of Science and Technology
Shenzhen 518055, P. R. China

Q. Xu
Institute for Integrated Cell-Material Sciences (WPI-iCeMS)
Kyoto University
Yoshida, Sakyo-ku, Kyoto 606-8501, Japan

DOI: 10.1002/adfm.202414537

diffusion of atoms, resulting in the growth and aggregation of particles. In recent years, researchers have made significant efforts to prepare ultrasmall HEA NPs,[6] while more efficient approaches are still being found in the way. Among the synthetic strategies, the spatial immobilization strategy possesses great merits. For instance, specific anchor sites on well-defined open support skeletons can spatially immobilize the NPs, decreasing their aggregation and thus endowing them with a uniform distribution.[7] For the sake of excellent catalytic performance, catalysts with open structures, such as abundant pore structures, are conducive to the fast mass transfer process, which can ensure the timely supplement of reactants and the release of the discharge products during the catalytic process. Especially for the cathode in ZABs, the electrocatalyst and the air electrode constitute the reaction environment of the gas–solid–liquid triple-phase interface, in which the surface/interface properties of the electrocatalyst play a pivotal role in the kinetic activity of both ORR and OER.[8] Therefore, great efforts should be made to elaborately design open support skeletons for well dispersing the HEA NPs and accelerating the mass transfer process.

Metal–organic framework (MOF)-derived porous nitrogen-doped carbon skeletons, such as ZIF-8-derived nitrogen-doped carbon (denoted as NC), can be used as an effective support to disperse and stabilize metal NPs due to their strong affinity to metal NPs, excellent conductivity, stable 3D porous structure, high surface area, and so on.[9] However, ZIF-8-derived NC contains mainly micropores, having insufficient spatial room for dispersing NPs, thus still resulting in NP aggregation and unfavorable slow mass transport during the catalytic processes. To address such a thorny issue, 3D hierarchically ordered porous nitrogen-doped carbon (HOPNC) skeleton connected by micro-, meso-, and macropores has been recently constructed to well disperse ultrasmall NPs and reduce mass transfer resistance simultaneously due to the highly open spatial structure and interconnected channels.[10]

Herein, we report an ultra-rapid Joule heating process to synthesize highly dispersed ultrasmall PtPdFeCoNi HEA NPs with a size of ≈2 nm and randomly distributed multimetallic single atoms simultaneously, which are spatially immobilized on the 3D hierarchically ordered porous nitrogen-doped carbon skeleton (denoted as PtPdFeCoNi/HOPNC). Thanks to the spatial immobilization of the HEA NPs and multimetallic single atoms on the 3D HOPNC skeleton and the successful construction of interconnected channels for fast mass transfer, the as-prepared PtPdFeCoNi/HOPNC exhibits superior bifunctional electrocatalytic performances with a positive half-wave potential ($E_{1/2}$) of 0.866 V versus RHE for ORR, a low overpotential of 310 mV at 10 mA cm^{-2} for OER, and favorable ORR/OER kinetic characteristics. Furthermore, PtPdFeCoNi/HOPNC-based ZAB exhibits excellent rate performances and cycling stability, surpassing those of commercial Pt/C-RuO_2-based ZAB. This work not only enriches the recipes of maximizing the utilization of multiactive sites of oxygen electrocatalysts and boosting the reaction kinetics but also sheds light on the rational design and synthesis of efficient oxygen electrocatalysts toward broad applications for energy storage and conversion systems.

2. Results and Discussion

2.1. Synthesis and Characterizations of Electrocatalysts

The synthesis of the PtPdFeCoNi/HOPNC is schematically illustrated in **Figure 1**. Briefly, 3D ordered polystyrene sphere (PS) templates were added into the saturated methanolic solution containing 2-methylimidazole and $Zn(NO_3)_2{\cdot}6H_2O$, and then a blended $CH_3OH/NH_3{\cdot}H_2O$ solution was added to induce the generation of ZIF-8 crystalline phase (ZIF-8@PS).[11] Afterward, 3D hierarchically ordered porous ZIF-8 (denoted as HOP-ZIF-8) was successfully fabricated after removing the PS templates (Figure S1a, Supporting Information). The powder X-ray diffraction (PXRD) pattern shows that all the characteristic peaks of HOM-ZIF-8 match well with those of ZIF-8 and simulated ZIF-8 (Figure S1b, Supporting Information). No peaks corresponding to PS were detected, further demonstrating that the PS templates were completely removed. A highly conductive HOPNC support with well-defined polyhedral morphology was obtained after further carbonization of HOP-ZIF-8 (Figure S2a, Supporting Information). Meanwhile, metal ions could be easily absorbed on HOPNC through a wet impregnation method owing to the existence of abundant micropores in HOPNC.[10a] Finally, ultrasmall PtPdFeCoNi HEA NPs and multimetallic single atoms spatially immobilized on HOPNC (PtPdFeCoNi/HOPNC) were successfully synthesized through Joule heating process (Figure S2b, Supporting Information), during which metal ions could be converted to form ultrasmall HEA NPs and multimetallic single atoms in a short time.[12] The typical scanning electron microscopy (SEM) images indicate that PtPdFeCoNi/HOPNC displays a uniform polyhedral structure with abundant ordered macropores with pore sizes ranging from ≈ 80 to 110 nm (**Figure 2a**; Figure S3a, Supporting Information). Meanwhile, the SEM and high-angle annular dark-field scanning transmission electron microscopy (HAADF-STEM) images suggest that the macropores of carbon support are interconnected by mesopores (Figures S3b–d, Supporting Information). These properties are favorable to the mass transfer during the electrocatalytic processes.[13] Besides, NC support derived from ZIF-8 was also fabricated. The PXRD patterns and Raman spectra of HOPNC and NC are similar, indicating the degree of graphitization between them is almost the same (Figure S4, Supporting Information). The SEM images show that the obtained NC support loaded with PtPdFeCoNi HEA NPs (denoted as PtPdFeCoNi/NC) inherits the rhomboid-shaped dodecahedron morphology of NC without apparently visible pore structure (Figure S5, Supporting Information). Besides, the commercial XC-72R was also used as a support to load PtPdFeCoNi HEA NPs (denoted as PtPdFeCoNi/XC-72R) for further comparison. The SEM images shown in Figure S6 (Supporting Information) indicate that PtPdFeCoNi/XC-72R displays no obvious morphological change compared with XC-72R.

TEM was further performed to reveal the unique microstructure of the as-prepared catalysts. As shown in Figure 2b,c, PtPdFeCoNi HEA NPs are uniformly dispersed on the HOPNC support with a mean size of ≈ 2.10 nm according to the particle size statistics. Surprisingly, in addition to the PtPdFeCoNi HEA NPs, plenty of multimetallic single atoms can also be identified on the HOPNC matrix, as manifested by the atomically

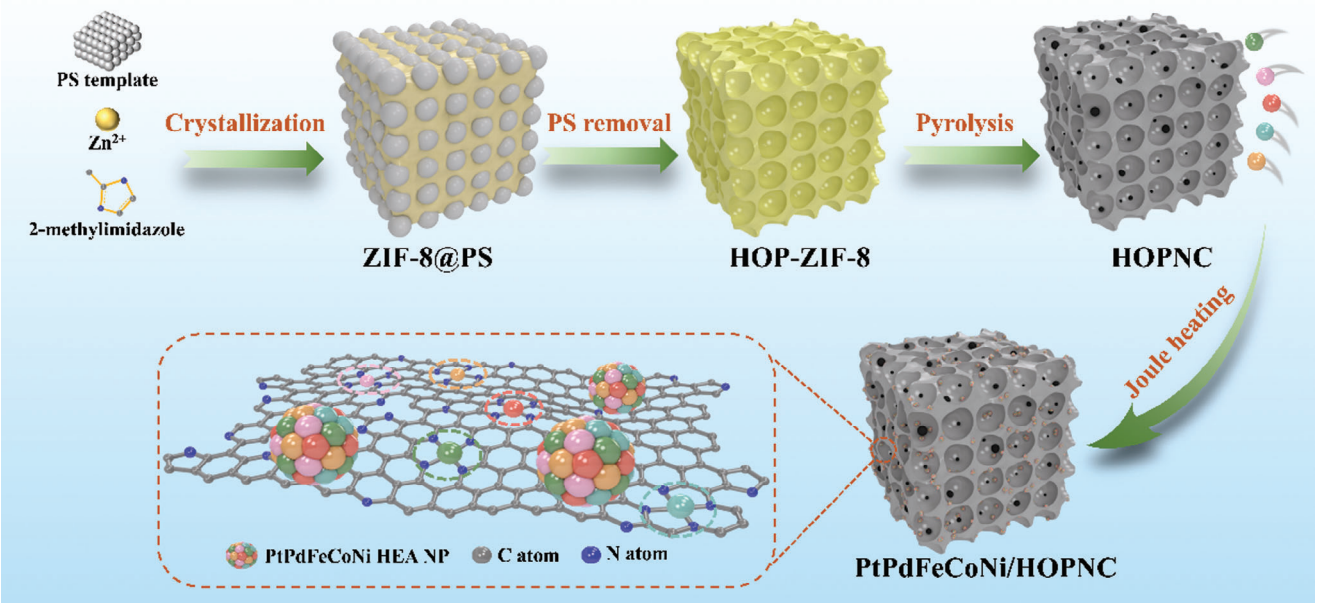

Figure 1. Schematic illustration of the preparation of PtPdFeCoNi/HOPNC.

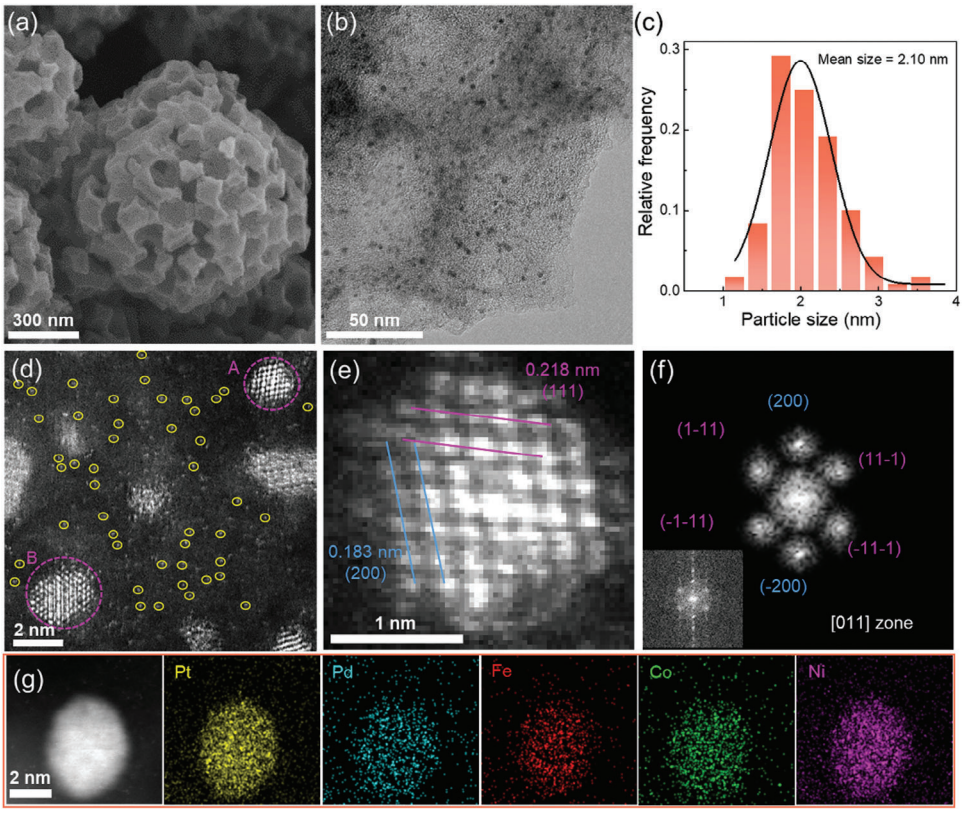

Figure 2. a) SEM image, b) TEM image and c) corresponding particle size distribution, d) HAADF-STEM image, e) atomically resolved HAADF-STEM image of region A in (d), f) corresponding FFT filtered image of region B in (d) (Inset: corresponding FFT pattern), g) HAADF-STEM image and corresponding EDX elemental mapping images of PtPdFeCoNi/HOPNC.

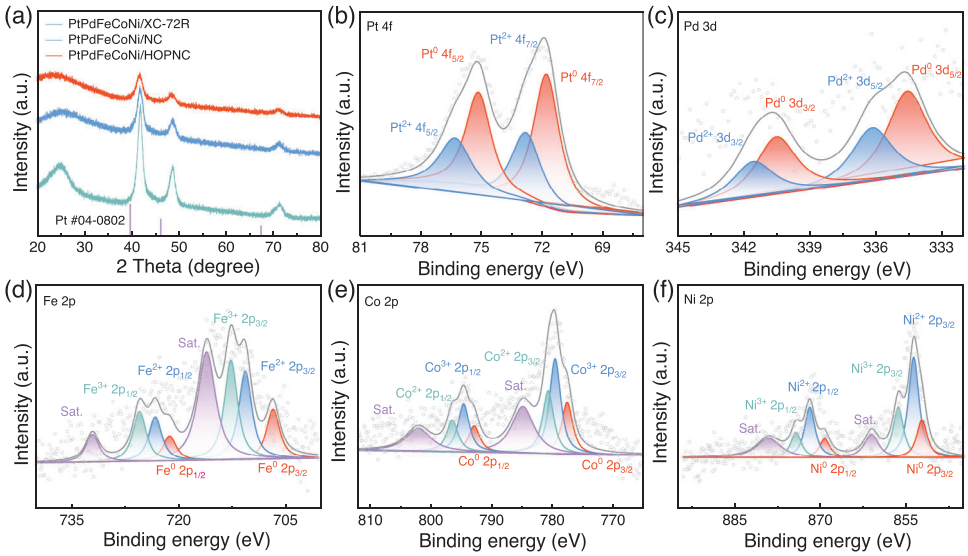

Figure 3. a) PXRD patterns of the as-prepared catalysts. High-resolution XPS spectra of b) Pt 4f, c) Pd 3d, d) Fe 2p, e) Co 2p, and f) Ni 2p for PtPdFeCoNi/HOPNC.

resolved HAADF-STEM image (Figure 2d) where they are highlighted by yellow circles. In contrast, PtPdFeCoNi HEA NPs with a mean size of ≈6.74 nm are densely dispersed on the external surface of the NC support (Figure S7, Supporting Information). As shown in Figure S8 (Supporting Information), PtPbFeCoNi HEA NPs and plenty of multimetallic single atoms also coexist in PtPdFeCoNi/NC. However, a very wide particle size distribution was observed in PtPdFeCoNi/XC-72R, ranging from a few to tens of nanometers. HAADF-STEM and corresponding EDX elemental mapping images of PtPdFeCoNi/XC-72R further confirm the coalescence phenomenon of HEA NPs (Figure S9, Supporting Information). The appearance of abnormally large HEA NPs indicates the occurrence of Ostwald ripening, resulting in severe sintering.[14] The above results indicate that HOPNC support plays a significant role in the spatial immobilization of the HEA NPs, thereby leading to the uniform distribution and maximized exposure of active sites. The HAADF-STEM image shown in Figure 2e exhibits the lattice spaces of 0.218 and 0.183 nm, which correspond to the (111) and (200) planes of the face-centered cubic (FCC) phase of Pt, respectively. The fast Fourier transformation (FFT) pattern shown in Figure 2f also demonstrates that the PtPdFeCoNi HEA NP is a typical FCC structure, in which the pattern is indexed to a zone axis of [011] with the diffraction planes of {111} and {200}. The energy dispersive X-ray spectroscopy (EDX) elemental mapping images show that the Pt, Pd, Fe, Co, and Ni elements are uniformly distributed in a single nanoparticle for PtPdFeCoNi/HOPNC (Figure 2g). According to the inductively coupled plasma optical emission spectroscopy (ICP-OES) analysis, the total metal loading for PtPdFeCoNi/HOPNC is 12.10 wt.%, and the content of each metal is shown in Table S1 (Supporting Information).

The PXRD patterns reveal that the as-prepared catalysts display a typical FCC structure (**Figure 3**a). The peaks located at 41.9°, 48.6°, and 71.2° correspond to the (111), (200), and (220) planes of FCC phase, respectively.[15] It should be noted that the peak positions of PtPdFeCoNi HEA shift to a higher angle than those of standard Pt (JCPDS No. 04–0802), indicating that PtPdFeCoNi HEA formed by alloying five hetero-principal elements with different atomic radii exists a certain compressive strain.[16] Obviously, the characteristic peaks of PtPdFeCoNi/XC-72, PtPdFeCoNi/NC, and PtPdFeCoNi/HOPNC become wider sequentially, indicating that the size of PtPdFeCoNi HEA NPs decreases successively.[14] This result matches well with the statistics of HAADF-STEM images and further indicates that the support plays a vital influence on the size of the formed HEA NPs. X-ray photoelectron spectroscopy (XPS) was applied to determine the surface composition and elemental state of the catalysts. High-resolution XPS spectra shown in Figures 3b–f indicate that Pt, Pd, Fe, Co, and Ni exist in both metallic and oxidation states. The presence of oxidation state might be caused by the surface oxidation of PtPdFeCoNi/HOPNC when exposed to air.[17] Besides, the appearance of C–N in the high-resolution XPS spectrum of C 1s and pyrrolic N, pyridinic N, and graphitic N in the high-resolution XPS spectrum of N 1s demonstrates that N atoms are successfully doped into the carbon framework in the HOPNC (Figure S10, Supporting Information).[18,19] The existence of pyridinic and pyrrolic N species in HOPNC contributes to strong interactions between metal species (i.e., NPs and single atoms) and substrate. This interaction helps to prevent the obvious aggregation of NPs and facilitates the formation of single atoms via metal-N bonding (Figure S10b, Supporting Information). This can also be vividly confirmed by the coalescence phenomenon of PtPdFeCoNi HEA NPs on XC-72R support, as there are no N species in XC-72R support.

The valence states and local coordination environments of Fe in PtPdFeCoNi/HOPNC were further measured through the X-ray absorption near-edge structure (XANES) and extended X-ray absorption fine structure (EXAFS) measurements. As shown in Figure S11a (Supporting Information), the Fe K-edge in PtPdFeCoNi/HOPNC exhibits a slight rightward shift compared with that of Fe foil, primarily due to the low electronegativity of Fe, which leads to an electron-deficient state. The Fourier transform

(FT) EXAFS spectra of Fe K-edge reveal the peaks ≈ 1.45 and 2.13 Å, which can be assigned to the Fe-N and Fe-metal scattering paths, respectively (Figure S11b, Supporting Information). The wavelet transform (WT) analysis also identifies the existence of both Fe–N and Fe-metal paths in PtPdFeCoNi/HOPNC (Figure S12a, Supporting Information), distinguishing them from those in Fe foil (Figure S12b, Supporting Information). The EXAFS fitting curves and the corresponding structural fitting parameters of the Fe K-edge indicate that the average coordination number for the Fe–N bonding configuration is 4.02, implying the presence of Fe-N_4 structure (Figure S13 and Table S2, Supporting Information). Besides, two different types of Fe-metal bonding configurations with bond lengths of 2.59 and 2.88 Å can be observed, corresponding to coordination numbers of 3.51 and 1.20, respectively. These characterizations further demonstrate the coexistence of multimetallic single atoms and HEA NPs for PtPdFeCoNi/HOPNC.

The in-depth investigation of porosity, including pore size distribution and specific surface area, was performed using N_2 adsorption/desorption analysis. As shown in Figure S14a (Supporting Information), the abrupt increase in the adsorption isotherm at relatively low pressure ($P/P_0 < 0.01$) for PtPdFeCoNi/NC can be used as a convincing proof for the high concentration of micropores, which are in favor of anchoring the isolated metal sites due to the resultant high specific surface area.[20,21] The combined type-I/IV isotherms of PtPdFeCoNi/HOPNC and HOPNC show high nitrogen adsorptions at lower pressure and the typical hysteresis loops, demonstrating the coexistence of micropores and mesopores (Figure S14a, Supporting Information). Moreover, no plateau was observed in the isotherms of PtPdFeCoNi/HOPNC and HOPNC when the P/P_0 value is close to 1, suggesting the existence of macroporous structure (Figure S14a, Supporting Information). It is believed that N_2 adsorption mainly depends on the micropores in the sample for the Brunauer–Emmett–Teller (BET) test. In general, the higher the N_2 adsorption, the larger the BET surface area. In our case, the similar surface areas of PtPdFeCoNi/HOPNC and PtPdFeCoNi/NC may be due to their similar micropores. The pore volume of PtPdFeCoNi/HOPNC is larger than that of PtPdFeCoNi/NC, which may be due to the existence of abundant mesopores and macropores in HOPNC in addition to micropores (Figure S14b, Supporting Information). The BET surface area of PtPdFeCoNi/HOPNC is slightly lower than that of HOPNC, indicating the reduction of micropores in HOPNC (Figure S14c, Supporting Information), probably because the loaded PtPdFeCoNi HEA NPs blocked part of the micropores in HOPNC. There is neither high nitrogen adsorption at low pressure nor a typical hysteresis loop for PtPdFeCoNi/XC-72R (Figure S14a, Supporting Information), demonstrating its low specific surface area and poor pore structure. Owing to the successful construction of highly open spatial architecture and interconnected channels, PtPdFeCoNi/HOPNC displays a higher pore volume of 1.03 $cm^3\ g^{-1}$ and a comparable specific surface area (902.14 $m^2\ g^{-1}$) compared with those of PtPdFeCoNi/NC (Figure S14c, Supporting Information). Due to the high pore volume of mesopores and macropores, more inner spaces are available for immobilizing NPs, resulting in the more uniform distribution of PtPdFeCoNi NPs immobilized both on the surface of inner spaces and on the outer surface of HOPNC, in contrast to the case of NC where NPs are immobilized only on the outer surface. Meanwhile, the abundant channels can also enable the PtPdFeCoNi/HOPNC catalyst to achieve a rapid mass transfer during the electrocatalytic process, thereby improving ORR and OER performances.

2.2. Electrocatalytic Performance Characterizations

The ORR performance of the as-prepared catalysts was first evaluated in O_2-saturated 0.1 M KOH solution. Notably, immobilizing ultrasmall PtPdFeCoNi NPs and multimetallic single atoms on HOPNC significantly enhanced the electrocatalytic activity. As shown in **Figure 4a**, the $E_{1/2}$ changes from 0.822 V for HOPNC to 0.866 V for PtPdFeCoNi/HOPNC, which demonstrates that the metal active sites play a vital role in excellent ORR activity. Furthermore, the $E_{1/2}$ of PtPdFeCoNi/HOPNC is comparable to that of the commercial Pt/C (0.868 V) and superior to those of PtPdFeCoNi/NC (0.852 V) and PtPdFeCoNi/XC-72R (0.827 V), demonstrating the outstanding electrocatalytic activity of PtPdFeCoNi/HOPNC electrode for ORR. Generally speaking, a small Tafel slope indicates an accelerated reaction kinetics. Obviously, PtPdFeCoNi/HOPNC was proved with the lowest Tafel slope (53.9 mV dec^{-1}) compared with those of PtPdFeCoNi/XC-72R (82.8 mV dec^{-1}), PtPdFeCoNi/NC (64.2 mV dec^{-1}), and benchmark Pt/C (63.1 mV dec^{-1}), indicating the fastest kinetic of PtPdFeCoNi/HOPNC toward ORR (Figure 4b). The kinetic current density (J_k) was extracted to further determine the kinetic process. As shown in Figure 4c, PtPdFeCoNi/HOPNC shows the highest J_k of 13.89 mA cm^{-2} at 0.85 V, which is much superior to those of commercial Pt/C (11.20 mA cm^{-2}), PtPdFeCoNi/NC (5.57 mA cm^{-2}), and PtPdFeCoNi/XC-72R (3.33 mA cm^{-2}). The excellent ORR kinetic of PtPdFeCoNi/HOPNC could be attributed to the hierarchically ordered porous structure, which is beneficial to accelerate the mass transfer during ORR process.[22] Besides, the rotating ring disk electrode (RRDE) measurement at 0.2–0.7 V versus RHE shows a lower H_2O_2 yield and higher electron transfer number (n) for PtPdFeCoNi/HOPNC than PtPdFeCoNi/NC (Figure 4d), indicating a higher selectivity on PtPdFeCoNi/HOPNC electrode. The corresponding Koutecky-Levich (K-L) plots exhibit good linearity between J^{-1} and $\omega^{-1/2}$ and similar slopes (Figure 4e), demonstrating the first-order reaction kinetic of PtPdFeCoNi/HOPNC for oxygen concentration.[2b] Meanwhile, the RRDE measurements and K-L plots consistently suggest an almost $4e^-$ ORR pathway for PtPdFeCoNi/HOPNC under alkaline condition.[23] Apart from the ORR activity, the long-term stability of PtPdFeCoNi/HOPNC was measured by an accelerated durability test. After 5000 cyclic voltammetry (CV) cycles, the $E_{1/2}$ of PtPdFeCoNi/HOPNC is almost the same as initial (Figure 4f), whereas there is obvious negative shift for the commercial Pt/C (Figure S15a, Supporting Information), indicating the superior electrochemical stability of PtPdFeCoNi/HOPNC against ORR. In addition, the methanol tolerance of PtPdFeCoNi/HOPNC was evaluated via chronoamperometry test. As shown in Figure S15b (Supporting Information), the commercial Pt/C displays a sharp current reduction after injecting 1 mL of methanol into O_2-saturated 0.1 M KOH, while PtPdFeCoNi/HOPNC exhibits a tiny current change, revealing its superb ability to resist methanol poisoning.

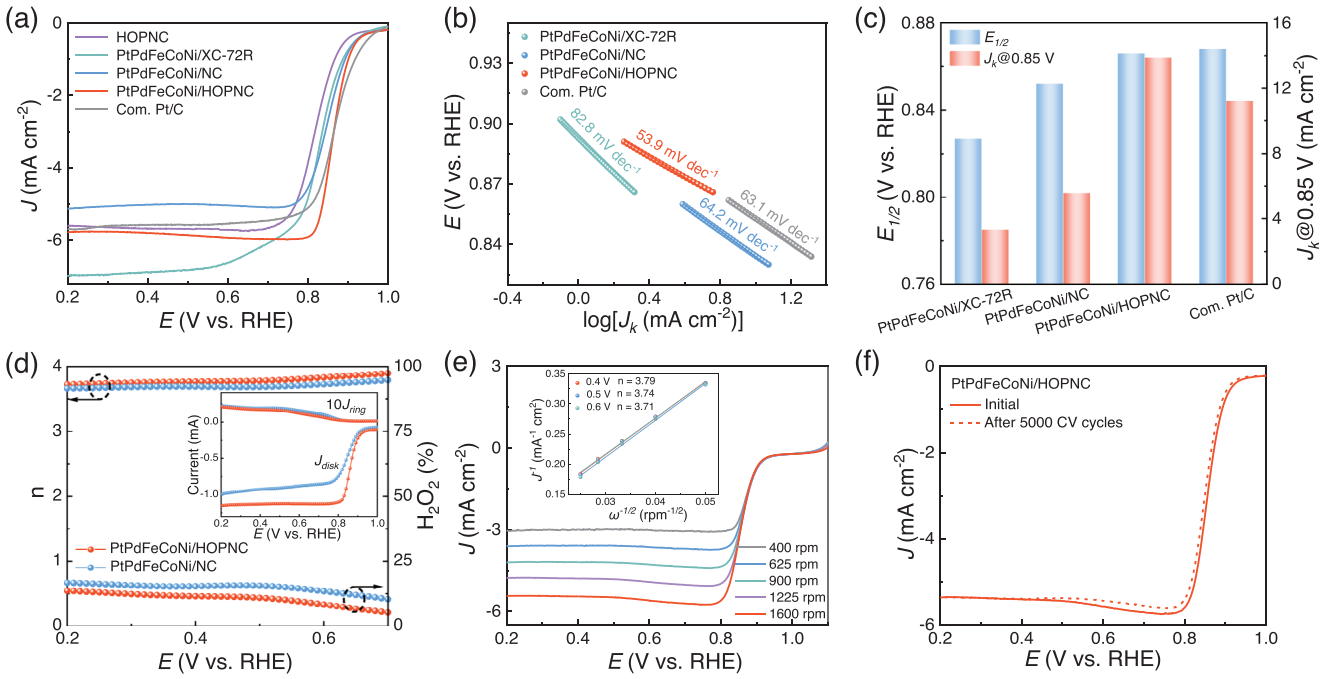

Figure 4. a) ORR polarization curves and b) corresponding Tafel slopes, c) $E_{1/2}$ and J_k, d) electron transfer number and H_2O_2 yield (Inset: corresponding RRDE measurement), e) LSV curves at different rotating speeds (Inset: corresponding fitted K-L plots), f) LSV curves before and after 5000 CV cycles of the as-prepared catalysts.

Furthermore, the OER performance of the as-prepared electrocatalysts was evaluated to assess the bifunctional catalytic ability. As shown in **Figure** 5a, the PtPdFeCoNi/HOPNC exhibits the lowest overpotential of 310 mV to achieve a current density of 10 mA cm^{-2}, which is superior to those of the commercial RuO_2 (322 mV), PtPdFeCoNi/NC (336 mV), and PtPdFeCoNi/XC-72R (373 mV), demonstrating a decent activity of PtPdFeCoNi/HOPNC electrode toward OER among the compared catalysts. In addition, PtPdFeCoNi/HOPNC requires the lowest overpotentials at the high current densities of 50 mA cm^{-2} and 100 mA cm^{-2} compared with PtPdFeCoNi/NC, PtPdFeCoNi/XC-72R, and commercial RuO_2 (Figure 5a; S16, Supporting Information). The outstanding catalytic activity of PtPdFeCoNi/HOPNC electrode at high current densities is probably caused by the abundant channels of HOPNC support, which enables it with excellent mass transfer ability. Moreover, Tafel slopes were further explored to evaluate OER kinetics. As shown in Figure 5b, PtPdFeCoNi/HOPNC affords the lowest Tafel slope of 88.7 mV dec^{-1} compared with those of commercial RuO_2 (179.6 mV dec^{-1}), PtPdFeCoNi/NC (114.7 mV dec^{-1}), and PtPdFeCoNi/XC-72R (133.9 mV dec^{-1}), suggesting the fastest OER kinetics process on PtPdFeCoNi/HOPNC electrode among the compared catalysts. Chronopotentiometry tests at 10 mA cm^{-2} were performed on PtPdFeCoNi/HOPNC and commercial RuO_2 to assess the catalytic stability. PtPdFeCoNi/HOPNC displays a much smaller potential change than commercial RuO_2 and can stably maintain over 40 h at a current density of 10 mA cm^{-2}, supporting its excellent OER stability (Figure 5c). The charge transfer rate during OER process was revealed by electrochemical impedance spectroscopy (EIS) test and the qualitative judgment could be made by the size of the semi-arc from the Nyquist plots. The result suggests that the charge transfer resistance (R_{ct}) of PtPdFeCoNi/HOPNC is the lowest among the compared catalysts (Figure 5d), which is consistent with the trend of OER activity. Electrochemically active surface areas (ECSAs) were further determined by the double-layer capacitance (C_{dl}) measurements in the non-Faradaic region (Figure S17, Supporting Information) to reflect the accessibility of active sites during the electrocatalytic reaction. As displayed in Figure 5e, PtPdFeCoNi/HOPNC shows a much higher C_{dl} value (20.36 mF cm^{-2}) than PtPdFeCoNi/NC (8.79 mF cm^{-2}) and PtPdFeCoNi/XC-72R (2.33 mF cm^{-2}), demonstrating that PtPdFeCoNi/HOPNC can maximize the exposure of active sites. Based on the promising ORR and OER performances of the as-prepared catalysts, the bifunctional performance was further quantified by the oxygen electrode activity parameter ($\Delta E = E_{J10} - E_{1/2}$), in which E_{J10} and $E_{1/2}$ represent the potential under the current density of 10 mA cm^{-2} for OER and the half-wave potential for ORR, respectively. As shown in Figure 5f, the calculated ΔE value for PtPdFeCoNi/HOPNC is 0.674 V, which is smallest among the control samples, even lower than that of commercial Pt/C-RuO_2 (0.684 V), revealing the excellent bifunctional activity of PtPdFeCoNi/HOPNC toward OER and ORR. It is noteworthy that the potential difference of PtPdFeCoNi/HOPNC is also smaller than or comparable to that of other reported bifunctional catalysts (Table S3, Supporting Information), further confirming its excellent bifunctional activity.

In order to distinguish the catalytic role of multimetallic single atoms and HEA NPs, the catalyst with multimetallic single atoms immobilized on HOPNC (MSAs/HOPNC) was synthesized. The PXRD pattern of MSAs/HOPNC is similar to that of HOPNC and no obvious characteristic peaks of metal nanoparticles were

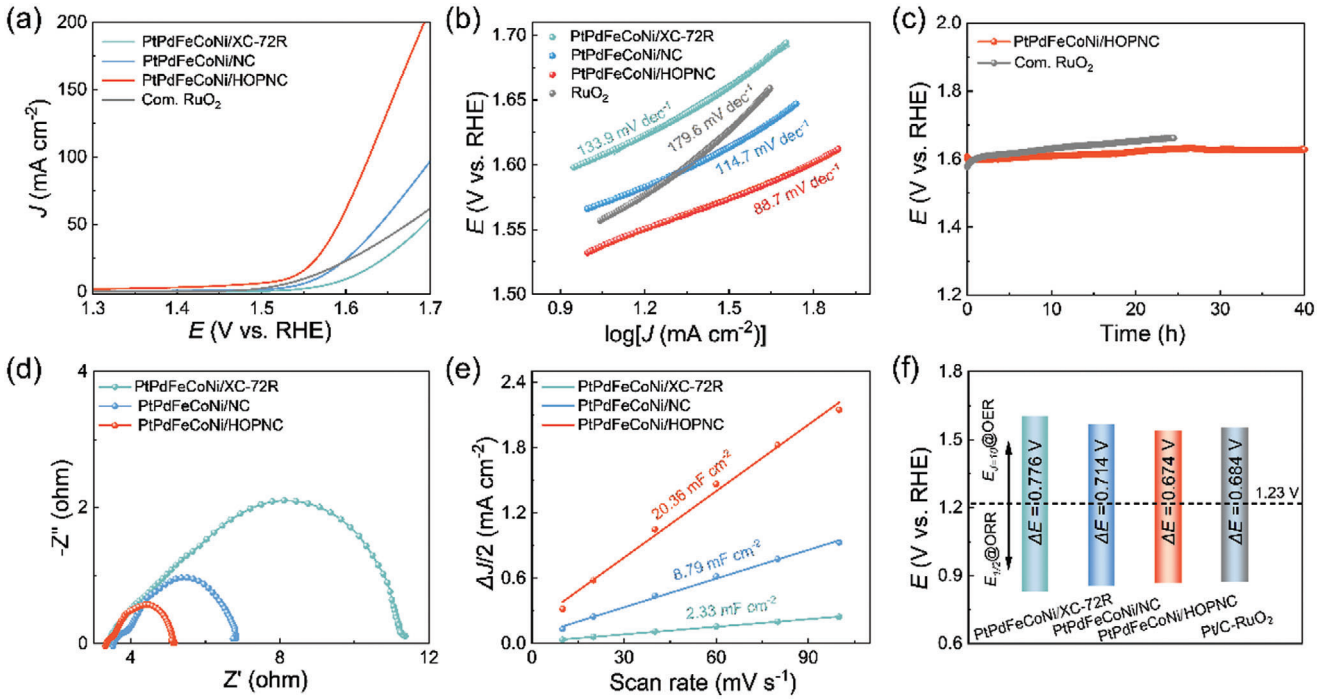

Figure 5. a) OER polarization curves and b) corresponding Tafel slopes, c) chronopotentiometry curves measured at a constant current density of 10 mA cm^{-2}, d) Nyquist plots, e) C_{dl}, and f) comparison of bifunctional activity of the as-prepared catalysts.

observed (Figure S18a, Supporting Information). HAADF-STEM image further suggests that the metal components loaded on HOPNC mainly exist in the form of single atoms (Figure S18b, Supporting Information). The catalytic performance results show that MSAs/HOPNC possesses outstanding ORR catalytic performance but not satisfactory OER catalytic performance compared with PtPdFeCoNi/HOPNC, indicating that the ORR and OER activities may be mainly from single atoms and nanoparticles, respectively (Figure S19, Supporting Information).

A quasi-solid-state ZAB using the transparent and robust hydrogel as an electrolyte was assembled by employing PtPdFeCoNi/HOPNC as the air cathode catalysts to further demonstrate its potential practical application (Figures S20a–d, Supporting Information). For comparison, another ZAB using a commercial Pt/C-RuO_2 mixture as the air cathode catalyst was also assembled and evaluated under the same condition. Notably, the PtPdFeCoNi/HOPNC-based quasi-solid-state ZAB can easily power up a commercial light-emitting diode light that displays "SUSTech" (Figure S20e, Supporting Information), indicating its promising application in microelectronic devices. As shown in **Figure** 6a, the PtPdFeCoNi/HOPNC-based ZAB displays an open-circuit voltage of ≈1.401 V, which is nearly as high as that of commercial Pt/C-RuO_2-based ZAB (1.405 V). The PtPdFeCoNi/HOPNC-based ZAB shows comparable discharging ability to commercial Pt/C-RuO_2 counterpart, but exhibits a much superior charging ability, meaning that PtPdFeCoNi/HOPNC-based ZAB can achieve a lower charge-discharge polarization (Figure 6b). The PtPdFeCoNi/HOPNC-based ZAB can achieve a peak power density of 233.94 mW cm^{-2} at a low current density of 273.3 mA cm^{-2} (Figure 6c). Additionally, the rate performance of PtPdFeCoNi/HOPNC-based ZAB was assessed via galvanostatic discharge tests with current densities ranging from 5 to 25 mA cm^{-2}. Figure 6d shows that PtPdFeCoNi/HOPNC-based ZAB can maintain a more stable and higher voltage plateau than Pt/C-RuO_2-based ZAB at high current densities (i.e., 15, 20, and 25 mA cm^{-2}), demonstrating the fast discharge process for PtPdFeCoNi/HOPNC-based ZAB. This might be attributed to the hierarchically ordered porous structure of PtPdFeCoNi/HOPNC electrocatalyst. The long-term rechargeable ability of PtPdFeCoNi/HOPNC- and Pt/C-RuO_2-based ZABs at 10 mA cm^{-2} was evaluated and the results are shown in Figure 6e. The continuous galvanostatic charge-discharge curve of PtPdFeCoNi/HOPNC-based ZAB demonstrates a negligible activity decay over 165 h of operation, revealing its excellent rechargeability. In contrast, Pt/C-RuO_2-based ZAB begins to decay sharply after ≈ 145 h. Hence, PtPdFeCoNi/HOPNC has the potential to replace the commercial Pt/C and RuO_2 as a bifunctional cathodic catalyst in ZAB.

3. Conclusions

In summary, highly dispersed ultrasmall PtPdFeCoNi HEA NPs and randomly distributed multimetallic single atoms were successfully spatially immobilized on 3D hierarchically ordered porous nitrogen-doped carbon skeleton via an ultra-rapid Joule heating process. The combination of strong metal anchor sites, hierarchical micro-/meso-/macroporosity, large specific surface area, and spacious pore volume was found to be crucial for achieving the special spatial immobilization effect, thus maximizing the exposure of the bifunctional electrocatalytic sites and ensuring fast mass transfer. The resultant PtPdFeCoNi/HOPNC exhibits superior bifunctional electrocatalytic performance with

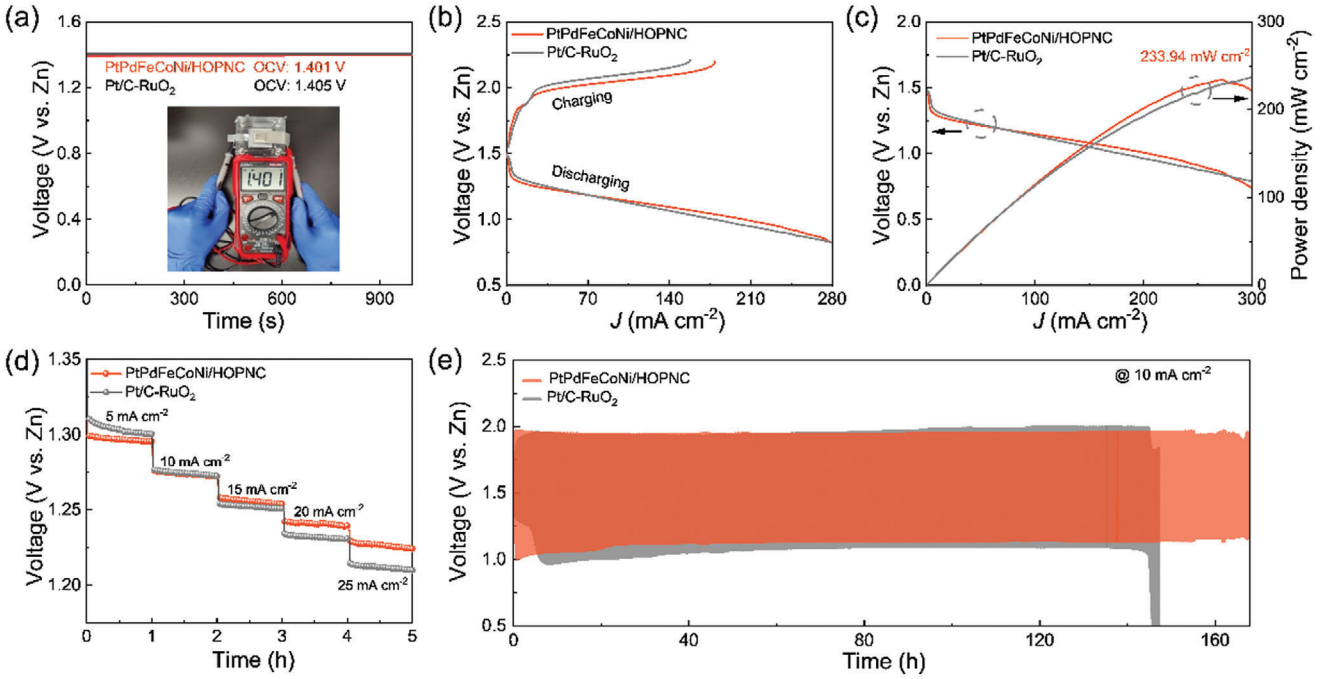

Figure 6. a) Comparison of open-circuit voltage curves, b) discharge and charge polarization curves, c) power density curves at discharging process, d) galvanostatic discharge curves at different current densities, and e) charge-discharge cycling performance of PtPdFeCoNi/HOPNC- and Pt/C-RuO_2-based ZABs.

a positive half-wave potential of 0.866 V vs RHE for ORR, a low overpotential of 310 mV at 10 mA cm^{-2} for OER, and favorable ORR/OER kinetic characteristics. Furthermore, PtPdFeCoNi/HOPNC-based ZAB exhibits excellent rate performances and cycling stability, outperforming those of Pt/C-RuO_2-based ZAB. The preliminary findings may significantly expand the scope of high-entropy catalysts due to the coexistence of highly exposed active sites and favorable mass transfer ability, and provide a universal strategy for rationally designing and synthesizing efficient electrocatalysts for various energy-conversion systems.

Supporting Information

Supporting Information is available from the Wiley Online Library or from the author.

Acknowledgements

The authors acknowledge the financial support of Guangdong Grants (2021ZT09C064), the Shenzhen Science and Technology Innovation Commission (GJHZ20220913142610020 and RCBS20231211090650087), National Key Research and Development Project (2022YFA1503900, 2023YFA1506601) and the Shenzhen Key Laboratory of Micro/Nano-Porous Functional Materials (SKLPM) (ZDSYS20210709112802010). The authors acknowledge the assistance of SUSTech Core Research Facilities. The authors acknowledge the assistance of the Shanghai Synchrotron Radiation Facility (SSRF).

Conflict of Interest

The authors declare no conflict of interest.

Data Availability Statement

The data that support the findings of this study are available from the corresponding author upon reasonable request.

Keywords

high-entropy alloy, multimetallic single atoms, ordered porous structure, spatial immobilization

Received: August 9, 2024
Revised: September 28, 2024
Published online:

[1] a) J.-S. Lee, T. Sun, R. Cao, N.-S. Choi, M. Liu, K. Lee, J. Cho, *Adv. Energy Mater.* **2011**, *1*, 34; b) S. Chu, Y. Cui, N. Liu, *Nat. Mater.* **2017**, *16*, 16.
[2] a) Q. Wang, S. Kaushik, X. Xiao, Q. Xu, *Chem. Soc. Rev.* **2023**, *52*, 6139; b) H. Pan, X.-L. Wang, F. Li, Q. Xu, *J. Mater. Chem. A* **2023**, *11*, 15006; c) M. Xie, X. Xiao, D. Wu, C. Zhen, C. Wu, W. Wang, H. Nian, F. Li, M. Gu, Q. Xu, *Nano Res.* **2024**, *17*, 5288.
[3] a) Q. Lu, X. Zou, Y. Bu, Z. Shao, *Energy Storage Mater.* **2023**, *55*, 166; b) J.-N. Liu, C.-X. Zhao, D. Ren, J. Wang, R. Zhang, S.-H. Wang, C. Zhao, B.-Q. Li, Q. Zhang, *Adv. Mater.* **2022**, *34*, 2109407.
[4] a) Q. Wang, Z. Zhao, Z. Zhang, T. Feng, R. Zhong, H. Xu, S. Pantelides, M. Gu, *Adv. Sci.* **2020**, *7*, 1901279; b) W. Zhang, J. Chang, G. Wang, Z. Li, M. Wang, Y. Zhu, B. Li, H. Zhou, G. Wang, M. Gu, Z. Feng, Y. Yang, *Energy Environ. Sci.* **2022**, *15*, 1573; c) Y. Li, Q. Zhang, X. Zhao, H. Wu, X. Wang, Y. Zeng, Q. Chen, M. Chen, P. Liu, *Adv. Funct. Mater.* **2023**, *33*, 2370105; d) S. Sarkar, A. Biswas, E. Siddharthan, R. Thapa, R. Dey, *ACS Nano* **2022**, *16*, 7890.

[5] a) E. George, D. Raabe, R. Ritchie, *Nat. Rev. Mater.* **2019**, *4*, 515; b) T. Batchelor, J. Pedersen, S. Winther, I. Castelli, K. Jacobsen, J. Rossmeisl, *Joule* **2019**, *3*, 834; c) Y. Yao, Q. Dong, A. Brozena, J. Luo, J. Miao, M. Chi, C. Wang, I. Kevrekidis, Z. Ren, J. Greeley, G. Wang, A. Anapolsky, L. Hu, *Science* **2022**, *376*, eabn3103; d) Y. Zhang, D. Wang, S. Wang, *Small* **2022**, *18*, 2104339.

[6] a) G. Feng, F. Ning, J. Song, H. Shang, K. Zhang, Z. Ding, P. Gao, W. Chu, D. Xia, *J. Am. Chem. Soc.* **2021**, *143*, 17117; b) J. Wang, J. Zhang, Y. Hu, H. Jiang, C. Li, *Sci. Bull.* **2022**, *67*, 1890; c) K. Huang, B. Zhang, J. Wu, T. Zhang, D. Peng, X. Cao, Z. Zhang, Z. Li, Y. Huang, *J. Mater. Chem. A* **2020**, *8*, 11938.

[7] a) A. Zhang, J. Xia, Q. Yao, Z. Lu, *Appl. Catal. B Environ.* **2022**, *309*, 121278; b) Z. Cai, I. Yamada, S. Yagi, *ACS Appl. Mater. Interfaces* **2020**, *12*, 5847; c) T. Li, S. Li, Q. Liu, J. Yin, D. Sun, M. Zhang, L. Xu, Y. Tang, Y. Zhang, *Adv. Sci.* **2020**, *7*, 1902371.

[8] T. Zhou, N. Zhang, C. Wu, Y. Xie, *Energy Environ. Sci.* **2020**, *13*, 1132.

[9] a) B. Liu, H. Shioyama, T. Akita, Q. Xu, *J. Am. Chem. Soc.* **2008**, *130*, 5390; b) S. Dang, Q.-L. Zhu, Q. Xu, *Nat. Rev. Mater.* **2017**, *3*, 17075; c) S. Chen, J. Duan, M. Jaroniec, S. Qiao, *Angew. Chem., Int. Ed.* **2013**, *52*, 13567; d) X. Wang, S. Hwang, Y.-T. Pan, K. Chen, Y. He, S. Karakalos, H. Zhang, J. Spendelow, D. Su, G. Wu, *Nano Lett.* **2018**, *18*, 4163; e) N. Du, C. Wang, R. Long, Y. Xiong, *Nano Res.* **2017**, *10*, 3228.

[10] a) J. Li, J. Liu, C. Chen, J. Guo, R. Bi, S. Chen, L. Zhang, M. Zhu, *Chem. Eng. J.* **2022**, *436*, 135186; b) Y.-L. Wu, X. Li, Y.-S. Wei, Z. Fu, W. Wei, X.-T. Wu, Q.-L. Zhu, Q. Xu, *Adv. Mater.* **2021**, *33*, 2006965; c) L. Jiao, X. Li, W. Wei, S.-H. Zhou, S.-G. Han, D.-D. Ma, Y. Mao, Q. Xu, X.-T. Wu, Q.-L. Zhu, *Appl. Catal. B Environ.* **2023**, *330*, 122638; d) N. Wang, X. Li, M.-K. Hu, W. Wei, S.-H. Zhou, X.-T. Wu, Q.-L. Zhu, *Appl. Catal. B Environ.* **2022**, *316*, 121667; e) X. Li, X.-T. Wu, Q. Xu, Q.-L. Zhu, *Adv. Mater.* **2024**, *36*, 2401926.

[11] K. Shen, L. Zhang, X. Chen, L. Liu, D. Zhang, Y. Han, J. Chen, J. Long, R. Luque, Y. Li, B. Chen, *Science* **2018**, *359*, 206.

[12] a) S. Lacey, Q. Dong, Z. Huang, J. Luo, H. Xie, Z. Lin, D. Kirsch, V. Vattipalli, C. Povinelli, W. Fan, R. Shahbazian-Yassar, D. Wang, L. Hu, *Nano Lett.* **2019**, *19*, 5149; b) Y. Yao, Z. Huang, L. Hughes, J. Gao, T. Li, D. Morris, S. Zeltmann, B. Savitzky, C. Ophus, Y. Finfrock, Q. Dong, M. Jiao, Y. Mao, M. Chi, P. Zhang, J. Li, A. Minor, R. Shahbazian-Yassar, L. Hu, *Matter* **2021**, *4*, 2340; c) Y. Liao, R. Zhu, W. Zhang, H. Zhu, Y. Sun, J. Chen, Z. Dong, R. Lv, *Nano Res.* **2024**, *17*, 3379.

[13] Z. Liu, Y. Du, R. Yu, M. Zheng, R. Hu, J. Wu, Y. Xia, Z. Zhuang, D. Wang, *Angew. Chem., Int. Ed.* **2023**, *62*, e202212653.

[14] T.-W. Song, C. Xu, Z.-T. Sheng, H.-K. Yan, L. Tong, J. Liu, W.-J. Zeng, L.-J. Zuo, P. Yin, M. Zuo, S.-Q. Chu, P. Chen, H.-W. Liang, *Nat. Commun.* **2022**, *13*, 6521.

[15] Y. Yu, F. Xia, C. Wang, J. Wu, X. Fu, D. Ma, B. Lin, J. Wang, Q. Yue, Y. Kang, *Nano Res.* **2022**, *15*, 7868.

[16] Z. Chen, J. Li, P. Ou, J. Huang, Z. Wen, L. Chen, X. Yao, G. Cai, C. Yang, C. Singh, Q. Jiang, *Nat. Commun.* **2024**, *15*, 359.

[17] a) K. Wang, R. Chen, H. Yang, Y. Chen, H. Jia, Y. He, S. Song, Y. Wang, *Adv. Funct. Mater.* **2024**, *34*, 2310683; b) M. Wei, Y. Sun, J. Zhang, F. Ai, S. Xi, J. Wang, *Energy Environ. Sci.* **2023**, *16*, 4009; c) R. Li, X. Liu, W. Liu, Z. Li, K. Chan, Z. Lu, *Adv. Sci.* **2022**, *9*, 2105808; d) J. Kwon, S. Sun, S. Choi, K. Lee, S. Jo, K. Park, Y. Kim, H. Park, H. Park, J. Jang, H. Han, U. Paik, T. Song, *Adv. Mater.* **2023**, *35*, 2300091.

[18] C.-C. Hou, L. Zou, Q. Xu, *Adv. Mater.* **2019**, *31*, 1904689.

[19] a) L. Yang, X. Zhang, L. Yu, J. Hou, Z. Zhou, R. Lv, *Adv. Mater.* **2022**, *34*, 2105410; b) Y. Wang, N. Katyal, Y. Tang, H. Li, K. Shin, W. Liu, R. He, M. Xu, G. Henkelman, S.-J. Bao, *Small* **2023**, *20*, 2306504; c) X. Lei, Q. Tang, Y. Zheng, P. Kidkhunthod, X. Zhou, B. Ji, Y. Tang, *Nat. Sustain.* **2023**, *6*, 816.

[20] X. Ao, L. Li, S. Yun, Y. Deng, W. Yoon, P. Wang, X. Jin, L. Dai, C. Wang, S.-J. Hwang, *Nano Energy* **2023**, *118*, 108952.

[21] X. Zhang, X. Han, Z. Jiang, J. Xu, L. Chen, Y. Xue, A. Nie, Z. Xie, Q. Kuang, L. Zheng, *Nano Energy* **2020**, *71*, 104547.

[22] X. Tang, Y. Wei, W. Zhai, Y. Wu, T. Hu, K. Yuan, Y. Chen, *Adv. Mater.* **2023**, *35*, 2208942.

[23] W. Yao, A. Hu, J. Ding, N. Wang, Z. Qin, X. Yang, K. Shen, L. Chen, Y. Li, *Adv. Mater.* **2023**, *35*, 2301894.